Fuel 365 (2024) 131217



Contents lists available at ScienceDirect

Fuel

journal homepage: www.elsevier.com/locate/fuel



Full length article

A computational chemistry study on the evolution of oxygen functional groups during char burnout

Özlem Yönder [a], Gunnar Schmitz [b,d], Rochus Schmid [c], Bastian Schnieder [a], Christof Hättig [a,*]

[a] Lehrstuhl für Theoretische Chemie I, Ruhr-Universität Bochum, D-44780, Bochum, Germany
[b] Lehrstuhl für Theoretische Chemie II, Ruhr-Universität Bochum, D-44780, Bochum, Germany
[c] Computational Materials Chemistry Group, Ruhr-Universität Bochum, D-44780, Bochum, Germany
[d] Research Center Chemical Sciences and Sustainability, Research Alliance Ruhr, D-44780, Bochum, Germany

ARTICLE INFO

Dataset link: https://doi.org/10.5281/zenodo.10514181

Keywords:
Combustion
Oxygen functional groups
Kinetic mechanism
Char oxidation

ABSTRACT

Oxygen functional groups (OFGs) within char play an important role during char burnout. They either already exist in the solid fuel and facilitate initiation reactions or they are formed as intermediates that open up fast reaction pathways with low barriers. This study aims to provide an atomistic-level understanding of the evolution of OFGs during char burnout. One of the major motivations behind this study is to provide functional group-specific reaction mechanisms which can be used to develop predictive physicochemical models of char oxidation. For our investigation of char burnout reactions at the OFGs, we use an automated reaction discovery tool based on reactive molecular dynamics simulations and quantum mechanical refinement of the reactions. The model OFGs comprise aldehydes, carboxylic acids, alcohols, anhydrides, quinones, furans, dioxins, pyrones, and lactones. We observe that radicals play an important role in initiating the combustion of these species. OFGs perturb the aromaticity of carbon rings and facilitate their opening and the decomposition into smaller carbon-containing species, such as CO, CO_2, formyl radicals and formaldehyde, leaving behind free radical sites, which can further react with less reactive gas-phase species such as O_2.

1. Introduction

Carbon capture, storage, and utilization technologies are crucial for achieving carbon neutrality targets to mitigate the irreversible impacts of climate change on ecosystems, biodiversity, and human systems. These technologies involve capturing carbon dioxide (CO_2) emitted from industrial processes, power plants, and other sources, and either storing it underground or utilizing it in other ways. One promising technology is oxy-fuel combustion, which involves burning fossil fuels with pure oxygen instead of air, producing a concentrated stream of CO_2 that can be captured easily. Therefore, the development of predictive models for solid fuel combustion reactions is of great importance for advancing oxy-fuel combustion carbon capture technologies. However, the combustion of solid fuels such as coal and biomass is complex and at an atomistic level poorly understood. Additionally, a detailed understanding of the underlying atomistic mechanisms is still lacking. To address this gap, this study aims to contribute to the microkinetic modeling of (bio)-char combustion, such as those presented in the physicochemical model of char oxidation in Ref. [1], by exploring reaction networks, with a particular focus on investigating the role of oxygen functional groups in the early steps of char combustion.

Oxygen functional groups (OFGs) play a crucial role in the oxidation of carbon-based fuels. They are already present in the solid fuel and accelerate initial combustion steps, but they are also formed as intermediates during combustion [2–4]. OFGs commonly found in chars include dioxins, phenols, lactones, pyrans, carboxylic acids, carboxylic anhydrides, peroxides, and cyclic ethers [5]. The molecular structure of (bio-)char consists of a mixture of pyrogenic amorphous carbon, turbostratic crystallites, and pore space [6]. It has been observed that amorphous chars include pyrones, anhydro sugars, phenols, furans, as well as small (poly)aromatic units [6]. At higher charring intensities, turbostratic crystallites are formed, preserving aromatic, aliphatic, and oxygen-containing components [6].

The evolution of the oxygen functional groups during the oxidation of carbon materials has also been investigated in several studies. X-ray absorption near-edge structure (XANES) spectra for three different carbon materials have shown that acenaphthylene char produces carbonyl-type and acid/anhydride-type surface complexes during oxidation, low-rank coal char containing phthalic anhydride and carboxylic acid functional groups forms aromatic ketones, and coal-char containing acid/anhydride species forms carbonyl species [7].

* Corresponding author.
E-mail address: christof.haettig@ruhr-uni-bochum.de (C. Hättig).

https://doi.org/10.1016/j.fuel.2024.131217
Received 28 October 2023; Received in revised form 19 January 2024; Accepted 13 February 2024
0016-2361/© 2024 The Author(s). Published by Elsevier Ltd. This is an open access article under the CC BY license (http://creativecommons.org/licenses/by/4.0/).

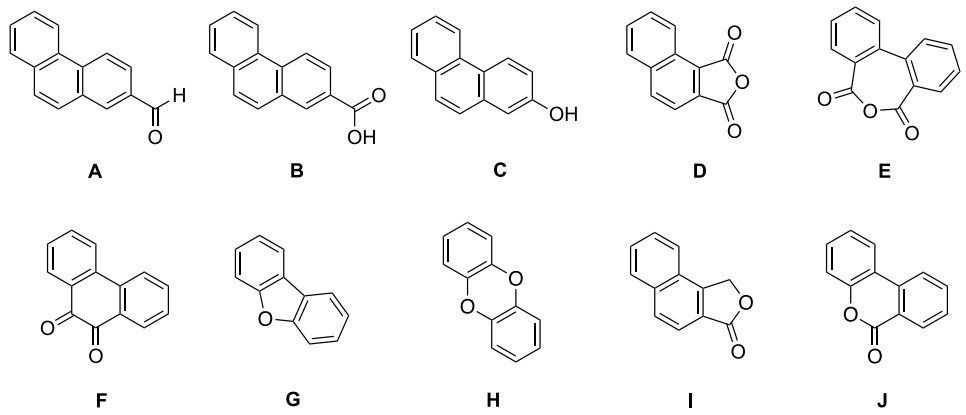


Fig. 1. The selected molecules to model different OFGs.

Temperature-programmed desorption experiments have also revealed that acidic groups like carboxyl groups and lactones release mainly CO_2 upon heating, whereas less acidic phenols, carbonyls, and pyrones release mainly CO or CO + CO_2 [5].

In this study, we investigate the combustion of selected phenanthrene-sized molecules with OFGs as shown in Fig. 1. Our aim is to gain an atomic-level understanding of the evolution of OFGs during char burnout, which can improve the accuracy and predictability of kinetic models of char oxidation. These molecules are chosen to prototype the combustion of aromatic building blocks of char near the common oxygen functional groups. These are in particular, phenanthrene-2-carbaldehyde (**A**) as an aldehyde, phenanthrene-2-carboxylic acid (**B**) as a carboxylic acid, phenanthrene-2-ol (**C**) as an alcohol, naphtho[1,2-c]furan-1,3-dione (**D**) and dibenzo[c,e]oxepine-5,7-dione (**E**) as examples for anhydrides, phenanthrene-9,10-dione (**F**) as a quinone, dibonzo[b,d]furan (**G**) as a furan; dibenzo[b,e][1,4]dioxine (**H**) as a dioxin, and naphtho[2,1-b]furan-2(1H)-one (**I**) and 6H-benzo[c]chromen-6-one (**J**) as examples for pyrones and lactones.

To explore the chemical space of combustion reactions, we employ reactive molecular dynamics (MD) simulations as they overcome the constraints imposed by chemical intuition and enable efficient automation. While systematic combinatorial approaches, such as the one proposed in Chemoton [8,9], would provide a complete exploration of possible elementary reaction steps, they are computationally not feasible for such complex systems. Reactive MD simulations provide an efficient alternative for reaction discovery that focuses on the most likely reaction pathways.

Among the methods which can be used for the purpose of reactive MD simulations, semi-empirical density functional theory is widespread. For instance, GFN2-xTB has been employed to simulate cyclohexane combustion by five dioxygen molecules [10]. On the other hand, reactive force fields can be employed at larger scales and thus realistic char models, such as those presented in Ref. [11], although it lacks information on the electronic structure. It has been shown that when combined with a refinement at the quantum chemistry level, the reactive force field ReaxFF [12,13] generates chemically intuitive reactions [14–16]. In the current study, we have used an automated workflow [16] that uses ReaxFF [12,13] to discover combustion reactions and refine them using quantum chemistry methods at the level of density functional theory (DFT) and coupled cluster (CC). The use of quantum chemistry refinement enables the computation of reaction and activation free energies that are essential to obtain the kinetic data needed for constructing kinetic models.

The following sections are structured as follows: First, we describe the details of the methodology in Section 2. The main findings are presented in Section 3, which includes a brief description of the composition of the combustion atmosphere and followed by the presentation of the initial steps of combustion for each OFG, including their mechanisms as well as the reaction and activation energies. Finally, the main conclusions are given in Section 4. The rate constants for reactions with a significant barrier are reported in Appendix A.

2. Methods

For the studied model systems, reactive molecular dynamics (MD) simulations were done with an in-house Python interface to the LAMMPS Molecular Dynamics Simulator [17] employing the re-implementation of the reactive Force-Field ReaxFF [18]. The ReaxFF simulations have been run using the "CHO" parameterization for combustion as published in Ref. [13], at 2000K via a Nosé–Hoover thermostat, with a step size of 0.1 fs for 500 000 time steps (0.5 ns) in a cubic simulation box with a side length of 20 Å. The simulation box always contained one molecule of the functionalized polyaromatic, 40 O_2 molecules, and 10 OH• radicals.

For each of the initial molecules 5 MD simulations were done and analyzed for the results reported below. For the analysis of the MD trajectories, the refinement of the electronic structure, the search of transition state structures and the corresponding minima, and the calculation of the reaction rate constants, we have used the automated workflow described in Ref. [16]. We have particularly focused on the reactions which occur near the OFGs. When a bond breaking/formation event detected at the ReaxFF level of theory could not be refined automatically (using density functional theory (DFT/TPSS-D3/SVP)), we investigated it manually, and only the rest of the steps have been done with the automated scheme [16].

The quantum chemical calculations for the refinement were performed with the TURBOMOLE program package [19] version 7.6 [20] and version 7.7 [21]. All DFT calculations included Grimme's D3 dispersion correction [22] and were done with the ridft and rdgrad modules of TURBOMOLE. For the initial refinement of the electronic structure, we used the TPSS meta GGA exchange–correlation functional [23] and the SVP basis set [24] together with the corresponding optimized auxiliary basis sets for the resolution-of-the-identity approximation from Ref. [25]. The final DFT calculations were done with the hybrid meta GGA exchange–correlation functional TPSSh [26] and the TZVP [27] basis set together with the corresponding optimized auxiliary basis sets for the resolution-of-the-identity approximation from Ref. [28]. The TPSSh/TZVP harmonic vibrational frequencies have been scaled with the factor of 0.9874 that was optimized for TPSSh/6-31+G(d,p) to fit the experimental zero-point vibrational energies (ZPE) [29].

To obtain accurate electronic energies, explicitly correlated coupled-cluster singles and doubles calculations with perturbative connected triples [30,31], CCSD(F12*)(T*), were carried out at the optimized TPSSh/TZVP geometries using TURBOMOLE's ccsdf12 module [19]. For these calculations we used restricted open-shell Hartree–Fock

(ROHF) reference wavefunctions that were obtained with the dscf module [32]. The cc-pVDZ-F12 orbital [33], density-fitting auxiliary [34,35], and complementary auxiliary basis sets [36] are used with the recommended exponent [33] $\gamma = 0.9$ for the correlation factor of the geminals, $\exp(-\gamma r_{12})$. Benchmark calculations and a comparison with experimental data for the H-abstraction reactions of benzene, naphthalene, and phenanthrene with H atoms carried out in Ref. [37] showed that this combination of methods provides an accuracy of about ±5 kJ/mol for reaction and activation energies, which is difficult to achieve otherwise for reactions of molecules with the size studied in the current work.

The reaction and activation energies provided in Section 3 at both levels of theories, i.e. TPSSh-D3/TZVP and CCSD(F12*)(T*)/cc-pVDZ-F12, include zero point vibrational energy contributions (E_{ZPE}) calculated at the TPSSh-D3/TZVP level of theory unless stated otherwise. The reaction energies are calculated as

$$E_{rxn} = \sum_{i}^{products} (E_{el,i} + E_{ZPE,i}) - \sum_{i}^{educts} (E_{el,i} + E_{ZPE,i}) \quad (1)$$

and the activation energies as

$$E_{act} = (E_{el,TS} + E_{ZPE,TS}) - \sum_{i}^{educts} (E_{el,i} + E_{ZPE,i}) \quad (2)$$

where E_{el} is the electronic energy and TS stands for transition state structure. For non-unimolecular reactions, the reaction and activation energies are calculated with respect to non-interacting educt or product species at infinite distance. For a few of the studied reactions the reactants can form intermediate van der Waals (vdW) complexes with binding energy larger than a subsequent activation barrier. In these cases the reference energy for non-interacting reactants results in "negative" activation barriers. For these cases, we also determined at the TPSSh-D3/TZVP level of theory the binding energies for the vdW complexes and the activation energies with respect to the vDW complex. These results are given in the tables below in parenthesis. An example for this is the H-abstraction from phenanthrene-2-carbaldehyde with a hydroxyl radical (A0 + OH• → A2 + H_2O), as can be seen in Table 1 where the activation energy with respect to the non-interacting reactants at the TPSSh-D3/TZVP level of theory is −16.8 kJ/mol. When the van der Waals complex of the reacting species is optimized and the activation energy is calculated with respect to the vdW complex of the educts, the value increases to 8.2 kJ/mol.

3. Results and discussion

3.1. Combustion atmosphere

Hydrogen abstraction reactions, especially with hydroxyl radicals, are very important during combustion reactions in generating reactive organic radicals or reactive intermediates such as alkyl or hydroperoxyl radicals or hydrogen peroxide [38,39].

$$RH + OH\bullet \rightarrow R\bullet + H_2O \quad (3)$$

$$ROH + OH\bullet \rightarrow RO\bullet + H_2O \quad (4)$$

$$ROH + O_2 \rightarrow RO\bullet + HO_2\bullet \quad (5)$$

$$ROH + HO_2\bullet \rightarrow RO\bullet + H_2O_2 \quad (6)$$

$$H_2O_2 \rightarrow 2OH\bullet \quad (7)$$

Although rarely during the initial stages of combustion, the formation of highly reactive atomic species is also observed in the reactive MD simulations. For example, in some trajectories an oxygen atom was formed via the reaction of two hydroxyl radicals,

$$OH\bullet + OH\bullet \rightarrow H_2O + O \quad (8)$$

or a hydrogen atom via decomposition of a hydroperoxyl radical.

$$HO_2\bullet \rightarrow H\bullet + O_2 \quad (9)$$

Both are known from experimental studies, see e.g. Ref. [39] and references therein. At later stages of combustion, also small species containing carbon atoms are observed in the combustion atmosphere such as CO, CO_2, formyl radicals, formic acid, formaldehyde, and other small hydrocarbons. Some of the elementary reaction steps which release these gases can also be seen in the following sections. For example, aldehydes release CO, formyl radicals, formic acid, and formate radicals (Section 3.2). Carboxyl acid, carboxylic anhydrides, and lactones release CO_2 (Sections 3.3, 3.5, and 3.9). These observations are in accordance with previous findings which suggest the release of CO_2 for more acidic groups such as carboxylic species and lactones, and the release of CO or CO/CO_2 mixtures [40] from less acidic phenols, carbonyls, and pyrones. At the end of the simulations, upon complete combustion, the atmosphere is mostly composed of H_2O, CO_2, and O_2.

In the following paragraphs we present the results for the initial steps of the oxidation of different OFGs. We usually present the oxidation mechanisms until they have lead to (a) a new OFG, (b) the removal of the OFG, or (c) the opening, shrinkage, or expansion of a first ring. For some examples we included a few additional steps to give an indication how the oxidation can continue, e.g. for phenantrene-2-carboxylic acid we included the addition of O_2 to the aryl radical as a general further step than can follow the formation of radical sites in the aromatic framework.

3.2. Aldehydes

The series of reactions that phenanthrene-2-carbaldehyde (**A**) underwent in the MD simulations is illustrated in Fig. 2. Table 1 provides the corresponding reaction and activation energies obtained after the refinement at the TPSSh-D3/TZVP ($E_{act,DFT}$ and $E_{rxn,DFT}$) and CCSD(F12*)(T*)/cc-pVDZ-F12 ($E_{act,CC}$ and $E_{rxn,CC}$) level of theories. The importance of aldehydes in combustion is known in the literature since a long time. Salooja has studied experimentally the ignition behavior of aliphatic aldehydes [41]. A mechanism for the pyrolysis and oxidation of benzaldehyde as a model for aromatic aldehydes has recently been proposed by Namsyl et al. based on experimental results [42]. Computational results at the level of DFT/B3LYP/6-311G* have recently been published by Qi et al. for phenylacetaldehyde [43].

Phenanthrene-2-carbaldehyde reacts initially mostly with OH• radicals which either coordinate to the aldehyde carbon atom or abstract the H atoms from the aldehyde group. The addition of OH• to the aldehyde group initiates unimolecular rearrangement reactions that lead to the release of formyl (CHO•) and formate (HCOO•) radicals, formic acid (HCOOH), but also of H_2O and CO. The aldehyde group can transform into other oxygenated functional groups (OFGs), such as alcohol (phenanthrene-2-ol, A6) and carboxylic acid (phenanthrene-2-carboxylic acid, A3). It has been previously established that oxidation of benzaldehyde forms benzoic acid at ambient temperature [3]. The presence of free OH• radicals in the combustion atmosphere may facilitate this process. Another significant intermediate in the oxidation of the aldehyde group is the 2-phenanthrenyl radical, A4.

The intermediate A2 can be formed in various ways, e.g., by directly abstracting the hydrogen atom with an OH• radical from the aldehyde group (A0 + OH• → A2 + H_2O) or by adding OH• to the aldehyde group and then dehydrating it in a second step. The former pathway has practically no barrier and should be the preferred pathway, which is in agreement with the reaction scheme proposed for the oxidation of benzaldehyde [3]. When the OH• radical attaches to the intermediate

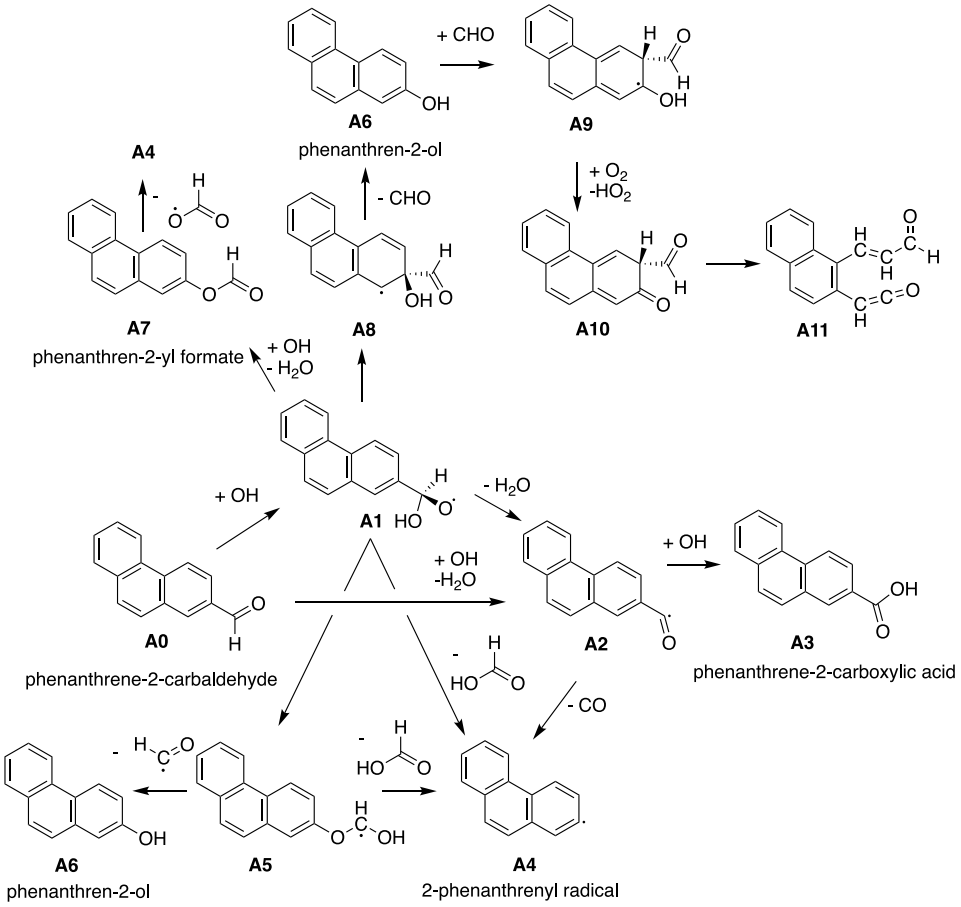


Fig. 2. The reactions of phenanthrene-2-carbaldehyde.

Table 1
TPSSh-D3/TZVP and CCSD(F12*)(T*)/cc-pVDZ-F12 results for reactions of phenanthrene-2-carbaldehyde in kJ/mol.

Reaction	$E_{act,\mathrm{DFT}}$	$E_{rxn,\mathrm{DFT}}$	$E_{act,\mathrm{CC}}$	$E_{rxn,\mathrm{CC}}$
A0 + OH• → A2 + H_2O	−16.8 (8.2)	−98.0	−11.3	−116.0
A0 + OH• → A1	9.0	−65.0	29.3	−54.5
A1 → A2 + H_2O	66.8	−32.6	99.1	−58.5
A2 + OH• → A3	Barrierless	−425.1		−451.6
A2 → A4 + CO	Barrierless	119.8		98.2
A1 → A4	39.6	29.2	43.3	20.6
A1 → A5	69.1	8.1	70.4	0.6
A5 → A6 + CHO•	155.6	10.1	171.6	3.6
A5 → A4 + HCOOH	69.8	21.1	91.2	20.0
A1 + OH• → A7 + H_2O	Barrierless	−386.9		−431.0
A7 → A4 + HCOO•	Barrierless	381.6		444.9
A1 → A8	72.3	19.8	110.7	1.4
A8 → A6	39.0	−3.0	58.4	1.5
A6 + CHO• → A9	24.8	−28.3	44.6	−30.8
A9 + O_2 → A10 + HO_2•	−8.7 (0.7)	17.2	44.2	99.7
A10 → A11	79.9	47.6	112.0	60.6

A2, phenanthrene-2-carboxylic acid A3 is produced with a high energy release of 451.6 kJ/mol.

The formation of the 2-phenanthrenyl radical (A4) occurred through four different pathways. The most favorable path is the removal of formic acid from intermediate A1, which leads to the formation of radical A4 with an activation barrier of 43.3 kJ/mol. Another pathway involves the rearrangement of the intermediate A1 to A5, followed by the release of formic acid (A5 → A4 + HCOOH). This pathway is less favorable because the latter step requires a relatively high activation barrier of 91.2 kJ/mol. The direct elimination of CO from the radical A2 is highly endothermic, requiring 98.2 kJ/mol energy. Lastly, A4 can be formed by oxidizing the intermediate A1 further to form phenanthrene-2-yl-formate (A7) very exothermically by −431.0 kJ/mol, followed by the elimination of the formate group highly endothermically by 444.9 kJ/mol.

3.3. Carboxylic acids

The reaction of aromatic carboxylic acids with radicals lead to the release of CO_2, similar as their thermal decomposition in pyrolysis [44]. While the pyrolysis can lead to the respective aryls or the aryl radicals, we find that when the decarboxylation is initiated by the attack of a radical preferentially the aryl radicals are formed. These aryl radical are known to react with molecular oxygen to peroxy radicals which open pathways for radical chain branching reactions [45,46].

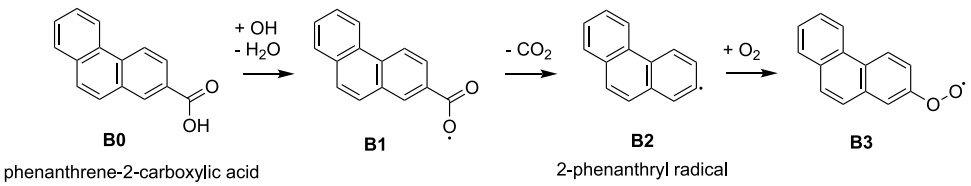


Fig. 3. The reactions of phenanthrene-2-carboxylic acid.

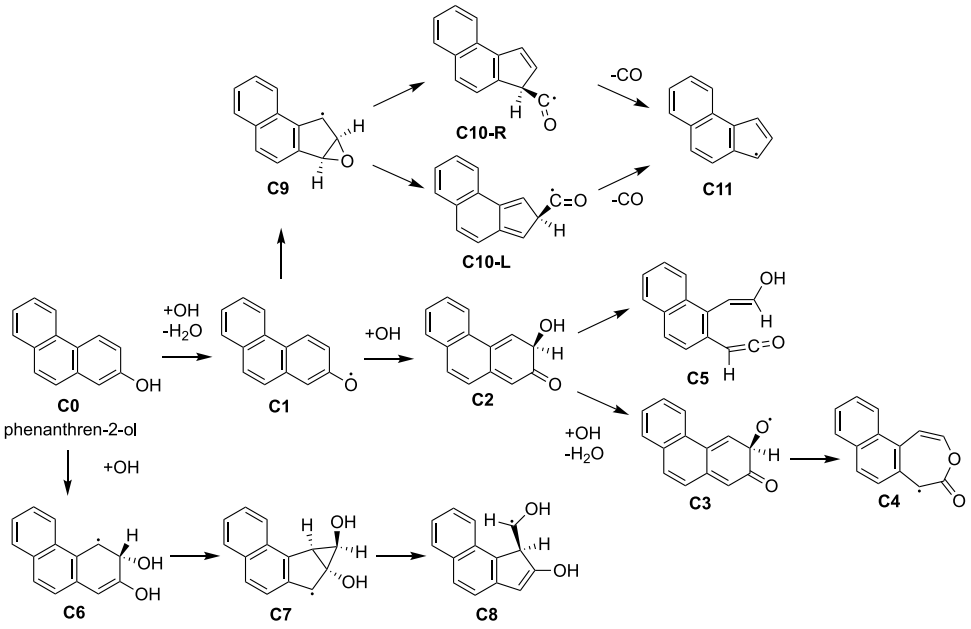


Fig. 4. The reactions of phenanthrene-2-ol.

Table 2
TPSSh-D3/TZVP and CCSD(T*)(F12*)/cc-pVDZ-F12 results for reactions of phenanthrene-2-carboxylic acid in kJ/mol.

Reaction	$E_{act,DFT}$	$E_{rxn,DFT}$	$E_{act,CC}$	$E_{rxn,CC}$
B0 + OH• → B1 + H_2O	Barrierless	−73.2		−42.3
B1 → B2 + CO_2	38.5	10.7	18.8	−24.5
B2 + O_2 → B3	Barrierless	−186.0		−190.4

In agreement with these observations, we find that Phenanthrene-2-carboxylic acid (**B**) reacts, e.g., with an OH radical exothermically releasing 42.3 kJ/mol energy, and hydrogen is abstracted from the OFG. Then the CO_2 is released forming the 2-phenanthryl radical (B2) with an activation barrier of 18.8 kJ/mol and a reaction energy of −24.5 kJ/mol. The latter radical can react, e.g., with molecular oxygen to a reactive organic peroxy radical (see Fig. 3 and Table 2).

3.4. Alcohols

As example for aromatic alcohols, we investigated the combustion of phenanthrene-2-ol (**C**). The reactions observed in the MD simulations are depicted in Fig. 4 and the corresponding reaction energies are given in Table 3. The oxidation of aliphatic alcohols has been studied a lot in the literature both experimentally and theoretically. Detailed mechanisms are available e.g. for ethanol [39] and *n*- and *iso*-propanol [47]

Similar as for aldehydes and carboxylic acids, also the combustion of phenanthrene-2-ol is initiated by the attack of a hydroxyl radical. It either abstracts a hydrogen from the hydroxyl group of phenanthrene-2-ol forming the corresponding phenolate radical C1, or is attached to the neighboring free carbon forming the intermediate C6. Both, the –OH and the −O• group perturb the aromatic π-system and thereby facilitate addition reactions at the α-C atom [37,48].

If to C1, in a consecutive step upon H-abstraction, another hydroxyl radical adds at the α-C atom, the closed-shell species C2 is formed. From the species C2, abstraction of another hydrogen atom leads to the formation of species C3, which then easily rearranges with an activation barrier of only 27.1 kJ/mol to species C4, which resembles a lactone, thereby releasing 160.7 kJ/mol energy (cmp. Fig. 4 and Table 3). Alternatively, if species C2 overcomes a barrier of 150.4 kJ/mol, the C–C bond between the two partially oxidized atoms (cmp. Fig. 4) can break to form in an endothermic reaction species C5 (see Table 3). Both species, C4 and C5, have one aromatic ring less than the original educt C0.

Energetically similar to the ring opening of C2, species C6 can rearrange and form species C7 with an activation barrier of 135.6 kJ/mol. At the following step, the three-membered ring opens with a smaller activation barrier of 49.7 kJ/mol releasing 12.8 kJ/mol energy. A reaction similar to this is the pathway leading to the release of CO from the oxyradical C1. This reaction has previously been studied for the phenoxy radical in great detail experimentally and theoretically [49,50]. In a previous systematic study, we have also investigated the effect of the polyaromatics' size and site type on reaction mechanisms and energies [37]. Here, we additionally present the CCSD(T) energies for the corresponding oxyradical, C1. The polycyclic radical C9 is formed by overcoming an activation barrier 193.5 kJ/mol, which is larger than that for the reaction of C6 to C7. The cyclo-propanone moiety of C9 opens to form species C10-R with an activation energy of 37.2 kJ/mol and releasing 63.2 kJ/mol energy. Subsequently, a CO molecule is eliminated from the carbonyl radical with a small activation barrier of 13.9 kJ/mol and an energy release of 105.8 kJ/mol.

Table 3
TPSSh-D3/TZVP and CCSD(T*)(F12*)/cc-pVDZ-F12 results for reactions of phenanthrene-2-ol in kJ/mol.

Reaction	$E_{act,DFT}$	$E_{rxn,DFT}$	$E_{act,CC}$	$E_{rxn,CC}$
C0 + OH• → C1 + H_2O	Barrierless	−129.5		−133.0
C1 + OH• → C2	Barrierless	−200.6		−231.2
C2 + OH• → C3 + H_2O	Barrierless	−43.0		−24.1
C3 → C4	18.9	−146.2	27.1	−160.7
C2 → C5	119.7	45.9	150.4	54.8
C0 + OH → C6	Barrierless	−77.9		−81.7
C6 → C7	128.1	87.7	135.6	94.4
C7 → C8	45.2	−4.7	49.7	−12.8
C1 → C9	183.0[a]	165.4[a]	193.5	173.2
C9 → C10-R	31.1[a]	−43.2[a]	37.2	−63.2
C10-R → C11 + CO	14.0[a]	−39.4[a]	20.8	−52.2
C9 → C10-L	54.0[a]	10.4[a]	58.1	−9.6
C10-L → C11 + CO	5.8[a]	−92.9[a]	13.9	−105.8

[a] The TPSSh-D3/TZVP structures and energies are taken from Ref. [37].

Table 4
TPSSh-D3/TZVP and CCSD(F12*)(T*)/cc-pVDZ-F12 results for reactions of naphtho[1,2-c]furan-1,3-dione in kJ/mol.

Reaction	$E_{act,DFT}$	$E_{rxn,DFT}$	$E_{act,CC}$	$E_{rxn,CC}$
D0 + H_2O → D2	128.5	1.6	160.5	7.6
D0 + H• → D1	72.8	−108.8	122.9	−85.1
D1 + OH• → D2	Barrierless	−374.5		−416.4
D2 + OH• → D3 + H_2O	Barrierless	−58.7		−22.4
D3 + OH• → D4-T + H_2O	Barrierless	−42.1		−11.5
D4-T → D5-T + CO_2	29.7	−14.9	11.4	−47.3
D5-T → D6-T + CO_2	56.4	31.5	31.7	−9.1
D3 + OH• → D4-S + H_2O	Barrierless	−41.5		−11.5[a]
D4-S → D5-S + CO_2	33.4	−242.4	34.0	−241.8[a]

[a] The CCSD(T) calculation of the open shell singlet D4-S species requires a two-determinant approach. However, because, at the unrestricted DFT/TPSSh-D3/TZVP level of theory, the singly occupied molecular orbitals of the D4-S look very similar to those of the D4-T (see Appendix B) and the energy difference between D4-S and D4-T is practically non-existent, one can draw the conclusion that the electrons in these orbitals are not interacting. Therefore, for the species D4-S, the ROHF-CCSD(T) energies of the D4-T are used, to calculate the CCSD(T) energies of the involved reactions.

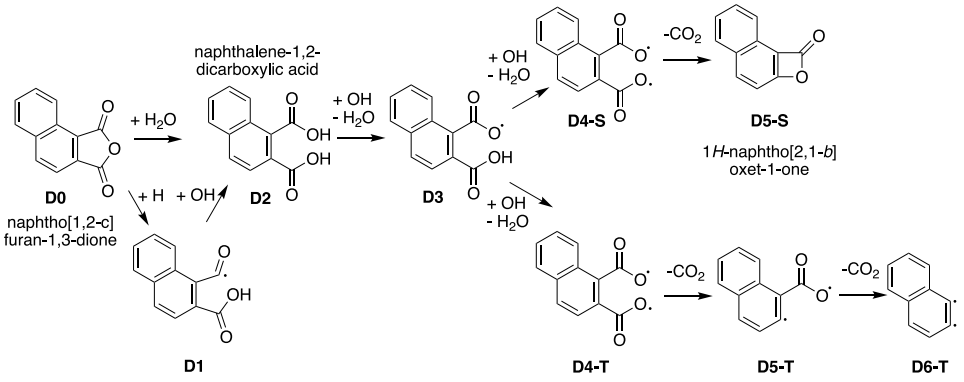


Fig. 5. The reactions of naphtho[1,2-c]furan-1,3-dione.

3.5. Anhydrides

We studied the combustion of two carboxylic anhydrides: Naphtho[1,2-c]furan-1,3-dione (**D**), also known as 1,2-naphthalic anhydride, features a 5-membered ring, and dibenzo[c,e]oxepine-5,7-dione (**E**), also known as 2,2'-biphenyl dicarboxylic anhydride, a non-planar molecule with the carboxylic anhydride functional group located in a 7-membered ring.

Carboxylic acids anhydrides are, compared to alcohols, aldehydes, and carboxylic acids, more difficult to oxydize. This is e.g. exploited in the synthesizes of phthalic acid anhydride by oxidation of *o*-xylene [51] or naphthalene [52].

As depicted in Fig. 5, we found in agreement with these observations for naphtho[1,2-c]furan-1,3-dione (D0), a higher analog of phthalic acid anhydride, at the anhydride group under combustion conditions only reactions that start with the formation of the respective dicarboxylic acid (D2) either by the direct addition of water or in a two-step mechanism via D1 by the consecutive addition of a H atom and an OH• radical. In gas phase, the direct addition of water requires an activation energy of 160.5 kJ/mol, as listed in Table 4. This reaction has been found during the quantum chemical refinement step and is not a reaction originally detected in the ReaxFF simulations. While searching for the transition state structure for the reaction D1 + OH• → D2, the initial structure converged during an optimization to the saddle point for D1 + H_2O → D2. The two-step mechanism via the intermediate D2 (see Fig. 5) involving the consecutive addition of a H atom and an OH• radical has a lower barrier of 122.9 kJ/mol, showing that the initiation via a radical addition is easier. But it requires of course that the corresponding radicals are present in the reaction atmosphere. During the combustion of organic fuels these radicals are formed e.g. through reactions (4)–(9) (see also Ref. [39]). Similar to the hydrogen abstraction from phenanthrene-2-carboxylic acid (B0 + OH• → B1 + H_2O), also the dicarboxylic acid D2 reacts with OH• radicals, leading after two consecutive H-abstractions to the formation

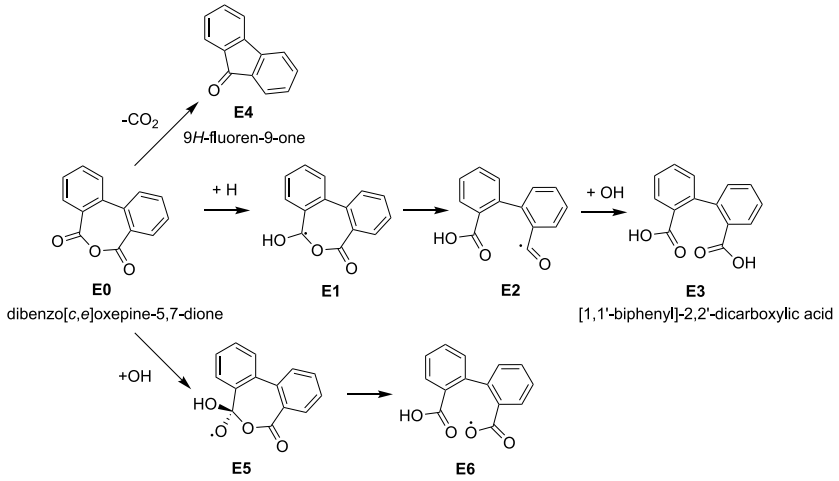


Fig. 6. The reactions of dibenzo[c,e]oxepine-5,7-dione.

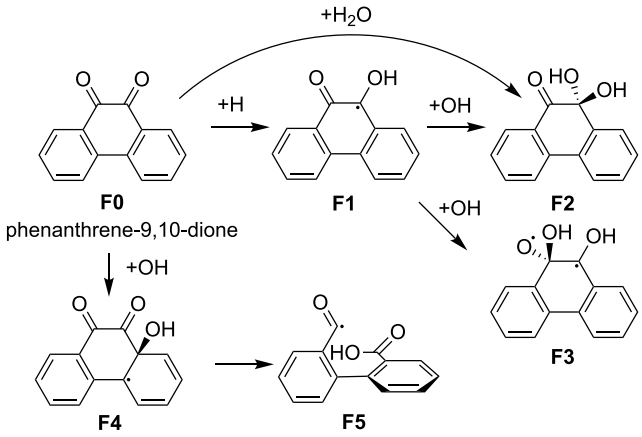


Fig. 7. The reactions of phenanthrene-9,10-dione.

Table 5
TPSSh-D3/TZVP and CCSD(F12*)(T*)/cc-pVDZ-F12 results for reactions of dibenzo[c,e]oxepine-5,7-dione in kJ/mol.

Reaction	$E_{act,DFT}$	$E_{rxn,DFT}$	$E_{act,CC}$	$E_{rxn,CC}$
E0 + H• → E1	7.9	−111.7	39.2	−90.4
E1 → E2	25.5	−11.2	44.5	−20.1
E2 → E3 + OH•	Barrierless	−415.6		−444.8
E0 → E4 + CO_2	177.4	−79.0	218.9	−72.7
E0 + OH• → E5	5.7	−37.7	30.6	−27.5
E5 → E6	11.3	−89.6	42.3	−64.8

of species D4. Since the spin 1/2 species D3 and a OH• radical (also spin 1/2) can couple to singlet or triplet spin states both of them have been investigated. The singlet (D4-S) and the triplet intermediate (D4-T) release both consecutively, two CO_2 molecules and form D5-S and D6-T, again similar to the phenanthrene-2-carboxylic acid (B1 → B2 + CO_2).

The reactions of dibenzo[c,e]oxepine-5,7-dione (**E**) is also initiated via a radical addition, as illustrated in Fig. 6. Specifically, the acyl group of E undergoes exothermic addition of a hydrogen atom to its oxygen atom, forming intermediate E1 with an activation energy of 39.2 kJ/mol, as indicated in Table 5. E1 then readily undergoes ring opening (E1 → E2) with a relatively low activation barrier of 44.5 kJ/mol. Upon reaction with an OH• radical, E2 forms a dicarboxylic acid (E3).

Alternatively, the attack of a hydroxyl radical at the anhydride group in dibenzo[c,e]oxepine-5,7-dione also leads to a ring-opening in a two-step mechanism. First, the intermediate E5 is formed exothermically with an activation energy of 30.6 kJ/mol releasing 27.5 kJ/mol energy. In the next step, the ring containing the anhydride group opens exothermically passing 42.3 kJ/mol of activation barrier and releasing 64.8 kJ/mol energy, leading to the formation of species E6.

In addition, ReaxFF simulations have indicated that dibenzo[c,e]oxepine-5,7-dione can release a CO_2 molecule directly, although this reaction has a higher activation barrier of 218.9 kJ/mol. If the direct CO_2 release reaction does occur, it leads to the formation of 9H-fluoren-9-one (E4), a ketone (see Table 5).

Table 6
TPSSh-D3/TZVP and CCSD(F12*)(T*)/cc-pVDZ-F12 results for reactions of phenanthrene-9,10-dione in kJ/mol.

Reaction	$E_{act,DFT}$	$E_{rxn,DFT}$	$E_{act,CC}$	$E_{rxn,CC}$
F0 + H_2O → F2	183.2	25.6	157.7	−30.4
F0 + H• → F1	Barrierless	−269.5		−250.0
F1 + OH• → F2	Barrierless	−224.7		−267.2
F1 + OH• → F3	36.6	17.0	60.6	25.9
F0 + OH• → F4	Barrierless	−60.4		−62.8
F4 → F5	57.8	−76.9	110.5	−74.5

3.6. Quinones

Quinones are known as important intermediates in the combustion of polycyclic aromatic hydrocarbons and an important contribution to atmospheric pollution that originates from combustion. Detailed reaction mechanisms are, however, only available for the benzoquinones as part of the combustion mechanisms for toluene [53] and benzene [54]. As example for quinone groups in PAHs, we investigated phenanthrene-9,10-dione (**F**) for which the reactions are shown in Fig. 7 and the energies are given in Table 6. Similar to the initiation reaction for the anhydride **D** (D0 + H_2O → D2), also the transition state structure for the reaction of phenanthrene-9,10-dione with a water molecule to species F2 was found during the quantum chemical refinement, while in the reactive MD simulation only the two-step pathway via the intermediate F1 was observed. The direct addition of H_2O to a carbonyl (C=O) group has a relatively high activation barrier of 157.7 kJ/mol. Along the radical pathway [55], a hydrogen atom is added in the first step to the oxygen of one of the carbonyl (C=O) groups, resulting in intermediate F1. This step is exothermic and practically barrierless, releasing 250.0 kJ/mol of energy. In the second step, OH• is added to the carbon of the C-OH group, leading to the formation of F2. This step is also practically barrierless and exothermic, releasing 267.2 kJ/mol of energy. Alternatively, the hydroxyl radical can add to the neighboring

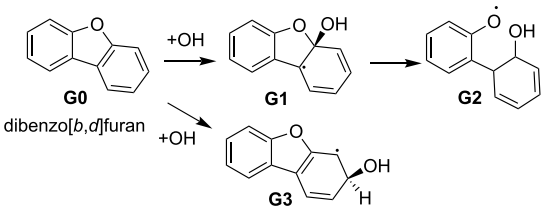


Fig. 8. The reactions of dibenzo[b,d]furan.

Table 7
TPSSh-D3/TZVP and CCSD(F12*)(T*)/cc-pVDZ-F12 results for reactions of dibenzo[b,d]furan in kJ/mol.

Reaction	$E_{act,DFT}$	$E_{rxn,DFT}$	$E_{act,CC}$	$E_{rxn,CC}$
G0 + OH• → G1	−5.1 (7.5)	−62.2	17.6	−67.1
G1 → G2	52.4	−40.6	75.4	−36.3
G0 + OH• → G3	Barrierless	−65.3		−70.5

carbonyl group and form species F3 with an activation energy of 60.6 kJ/mol and a reaction energy of 25.9 kJ/mol.

When OH• attacks the carbon located in a benzene ring next to the carbonyl (C=O) group, it forms intermediate F4 exothermically, releasing 62.8 kJ/mol of energy without significant barrier. Subsequently, the ring containing the quinone functional group breaks exothermically, releasing 74.5 kJ/mol of energy with a barrier of 110.5 kJ/mol. The preference for opening the middle ring, instead of the benzene ring, may be due to the fact that the middle ring is not aromatic and contains weaker carbon bonds. The resulting product, F5, contains an acyl radical site and a carboxylic acid functional group.

3.7. Furans

For studying the initial steps for combustion of furan compounds, i.e. systems with aromatic five-membered rings that contain an oxygen hetero atom in the ring, we used dibenzo[b,d]furan (**G**) as example (see Fig. 8 and Table 7). Furan itself and the alkyl-substituted derivatives 2-methylfuran (MF2) and 2,5-dimethylfuran (DMF) play important roles for liquid biofuels. Thus, their synthesis and combustion has recently attracted a lot of interest in the literature [56–60]. Less is known about the combustion pathways of furan groups in polycyclic aromatic hydrocarbons (PAHs). They have mostly been studied in the context of polychlorinated dibenzofurans (PCDFs) which are toxic and carcinogenic pollutants that can formed during waste incineration [61]. Marquaire et al. [62] proposed a mechanism for the oxidation of dibenzofuran with O_2 in the gas phase based on experimental data that was later refined by Ziegler-Devin et al. [63] and Tritz et al. [64] but without giving reaction rates or activation energies for the elementary steps.

For our model compound **G** we find that similar to the reaction F0 + OH• → F4 in quinones (**F**), a hydroxyl radical can add to the carbon next to the O atom in the furan ring, which then leads after a rearrangement reaction to the opening of the furan ring. However, in the furan the initial addition of the OH• radical at this site has a small barrier of 17.6 kJ/mol and is less exothermic, releasing 67.1 kJ/mol of energy, compared to the corresponding reaction in quinone (F) (see Fig. 11 and Table 10). Alternatively, OH• radicals can add to the benzene ring two positions further away, forming G3 in a barrierless exothermic reaction. In difference to the first pathway, the latter reaction happens barrierless. This is agreement with the mechanism proposed in Refs. [63,64] where the initial attack also happens preferentially at the carbon atoms that are not part of the furan ring.

Table 8
TPSSh-D3/TZVP and CCSD(F12*)(T*)/cc-pVDZ-F12 results for reactions of dibenzo[b,e][1,4]dioxine in kJ/mol.

Reaction	$E_{act,DFT}$	$E_{rxn,DFT}$	$E_{act,CC}$	$E_{rxn,CC}$
H0 + OH• → H1	Barrierless	−92.0		−94.8
H1 → H2	43.4	−33.3	72.8	−22.0
H3 → H4	35.0	12.8	40.5	6.9
H4 + OH• → H5	Barrierless	−222.8		−211.2
H5 → H6	32.1	−2.7	54.0	14.0
H6 → H7	7.5	−2.0	8.8	11.3
H7 → H8	137.3	116.1	148.3	100.4
H8 → H9 + H10	92.8	85.4	127.9	86.1

3.8. Dioxins

Similar as aromatic furans, also aromatic dioxins have in the literature mostly studied in the context of the environmental problems caused by the respective polychlorinated or polyflourinated compounds (PCDDs and PFDDs). Zeng et al. have reported in Ref. [65] a detailed mechanism for the first steps of the OH-initiated oxidation of di-fluorinated dibenzo[b,e][1,4]dioxine based on results from DFT calculations.

For (the non-haloginated) dibenzo[b,e][1,4]dioxine (**H**), which serves as example for dioxines, the addition of a hydroxyl radical at the carbon next to one of the oxygen heteroatoms (see Fig. 9) is, as for quinones barrierless. The addition of the hydroxyl radical leads in this case to intermediate H1 and is exothermic with an energy release of 94.8 kJ/mol (cmp. Table 8). Subsequently, the ring containing the oxygen atoms opens, forming H2 with an activation barrier of 72.8 kJ/mol and a reaction energy of −22.0 kJ/mol. This ring opening pathway resembles those observed for quinones (F0 + OH• → F4 → F5) and furans (G0 + OH• → G1 → G2). Both of these steps have also been found by Zeng et al. in Ref. [65] at the DFT level for the di-fluorinated compound with similar values for the reaction energies, however, with a small barrier for the initial OH• addition.

In one of the ReaxFF MD simulations the expoxide H3 was formed. This species rearranges into the oxepine H4 with a barrier of 40.5 kJ/mol. An OH• radical can then add without significant barrier to the carbon next to the O atom in the oxepine ring to form H5, thereby releasing 211.2 kJ/mol of energy.. After this radical addition, the ring containing the oxepine functional group can open in a rearrangement reaction with an activation barrier of 54.0 kJ/mol and a reaction energy of 14.0 kJ/mol. This ring-opening of the oxepine ring is again similar to the pathways observed for quinones, furans, and the dioxin group. The resulting intermediate, H6, rearranges to H7 and then undergoes another ring opening to form the species H8. The unimolecular reaction leading to H8 has a relatively large activation barrier of 148.3 kJ/mol and is endothermic by 100.4 kJ/mol. Following that, the species H8 can break into two fragments, one of which is cyclohexa-3,5-diene-1,2-dione (H10), also known as 1,2-benzoquinone. The other one, H9, is a reactive radical that undergoes further reactions. This reaction is endothermic by 86.1 kJ/mol with a high activation energy of 127.9 kJ/mol.

3.9. Lactones and pyrones

Lactones and pyrones are known intermediates in the atmospheric oxidation of aromatic hydrocarbons [66]. Thermodynamic and kinetic data for their oxidation is, however, scarce in the literature. Some results based on experimental and computational investigations are available for α-pyrone without annealed aromatic rings as part of a mechanism [67] for the combustion of furfural, a model for liquid biofuels.

For naphtho[2,1-b]furan-2(1H)-one (**I**), the example lactone chosen for this study, a direct release of CO_2 in a single reaction step (pathway

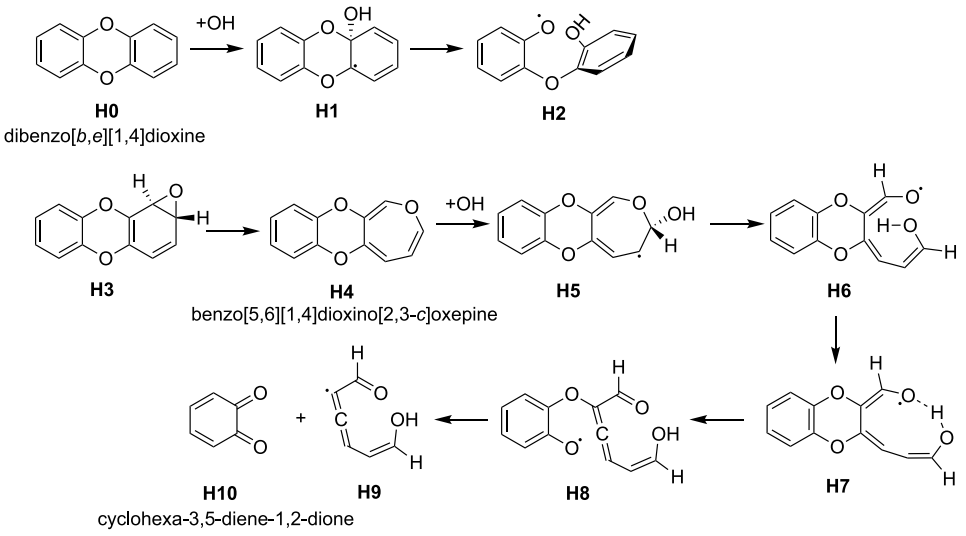


Fig. 9. The reactions of dibenzo[b,e][1,4]dioxine.

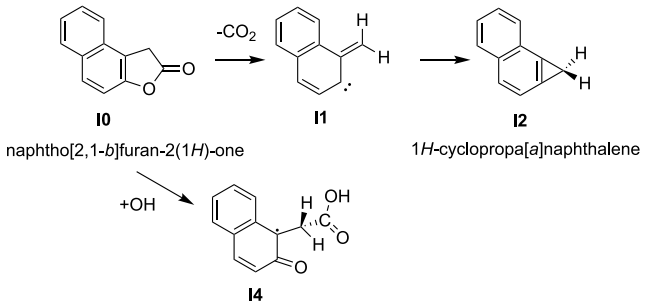


Fig. 10. The reactions of naptho[2,1-b]furan-2(1H)-on.

Table 9
TPSSh-D3/TZVP and CCSD(F12*)(T*)/cc-pVDZ-F12 results for reactions of naptho[2,1-b]furan-2(1H)-on in kJ/mol.

Reaction	$E_{act,DFT}$	$E_{rxn,DFT}$	$E_{act,CC}$	$E_{rxn,CC}$
I0 → I1 + CO_2	399.7	308.1	422.5	314.6
I1 → I2	3.9	−115.4	4.9	−107.7
I0 + OH• → I4	12.6	−161.6	65.9	−159.1

I0 to I1 in Fig. 10) was observed in one of the ReaxFF MD simulations. However, the refinement of the reaction pathway with electronic structure methods showed that for this reaction an activation barrier of 422.5 kJ/mol must be overcome (cmp. Table 9).

The most important pathway for the initial combustion steps of the lactone starts with the addition of OH• to the carbonyl C atom of the lactone group. For the lactone, this addition leads to a ring opening which forms the product I4 in the same elementary reaction step, with an activation barrier of 65.9 kJ/mol and a reaction energy of −159.1 kJ/mol.

As an example for pyrones, we investigated the combustion of 6H-benzo[c]chromen-6-one (**J**). The observed reactions are depicted in Fig. 11. Our results show that as for lactones the OH• radical attacks the carbon atom of the carbonyl (C=O) group which leads directly to an opening of the ring with the pyrone group, similar to what was found above for lactones. This reaction occurs as an initial step (pathway J0 → J6), but also after oxidation reactions at the aromatic rings that lead to a structure functionalized with a peroxide group in the bay region (pathway J4 → J5). As can be seen from the results listed in Table 10, the activation and reaction energies are similar for the two cases.

Table 10
TPSSh-D3/TZVP and CCSD(F12*)(T*)/cc-pVDZ-F12 results for reactions of 6H-benzo[c]chromen-6-one in kJ/mol.

Reaction	$E_{act,DFT}$	$E_{rxn,DFT}$	$E_{act,CC}$	$E_{rxn,CC}$
J0 + OH• → J6	23.9	−113.5	49.6	−113.8
J0 + O → J7	28.5	−110.8	68.2	−83.8
J0 + OH• → J1	Barrierless	−74.2		−75.8
J1 + O_2 → J2 + HO_2•	8.3	−9.1	43.4	−104.2
J2 + OH• → J3	Barrierless	−76.4		−75.7
J2 + OH• → J8 + H_2O	11.7	−12.6	34.3	−26.5
J4 + OH• → J5	21.4	−129.7	46.2	−131.4

The species J4 is formed through a pathway which is initiated by the addition of an OH radical to the benzene ring in meta position to the O atom in the pyrone ring. A hydrogen atom is then abstracted from J1 leading to an alcohol functional group in J2. Subsequently, another OH• radical can add at the neighboring bay region carbon and forms the species J3. Alternatively, the OH• radical can abstract a H atom at this position which leads to the aromatic radical J8.

4. Conclusions

In this study, we have investigated the atomistic combustion pathways of common oxygen functional groups existing within (bio)char using a combined reaction discovery workflow with reactive MD simulations together with an automated analysis using the findR software [16] and quantum mechanical refinement with density functional theory and coupled cluster calculations.

For the reaction discovery by ReaxFF simulations, we used a combustion atmosphere, containing the fuel model, molecular oxygen, and, in addition, hydroxyl radicals. To accelerate the reactive MD, it was run at elevated temperature and pressure. In general, in the MD simulations, a pool of additional small species is formed as reaction products from the oxygen molecules and OH• radicals such as HO_2•, H_2O_2, as well as H_2O. Although rarely, atomic oxygen and hydrogen were, after some time, present in the combustion atmosphere. In addition, the degradation of the fuel molecule produces carbon-containing species such as CO, CO_2, formaldehyde, formic acid, and other small hydrocarbons, but also reactive organic radicals, in particular formyl and formate radicals.

Less oxidized oxygen functional groups are often converted to more oxidized OFGs during the combustion. For example, the aldehyde group is easily oxidized to a carboxylic acid group, which can then decompose

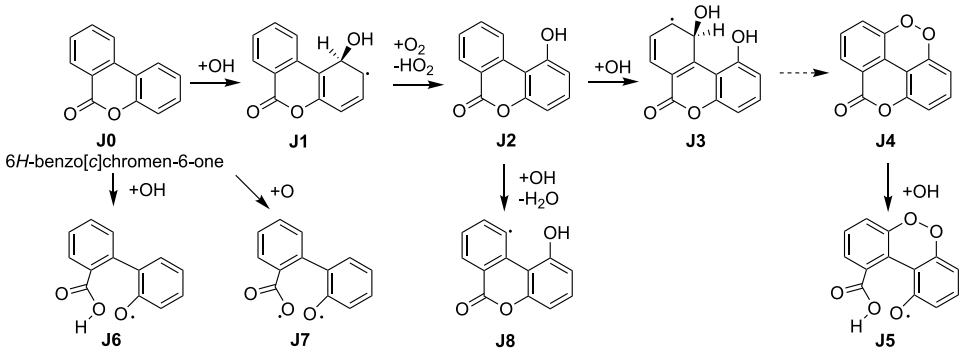


Fig. 11. The reactions of 6H-benzo[c]chromen-6-one.

under the release of CO_2. Such reactions generate free radical sites (R•) or, e.g. after the addition of a hydroxyl radical, alcohols (R-OH). In turn, alcohol groups can be oxidized e.g. to lactone-like species. Carboxylic anhydrides are transformed into dicarboxylic acid groups which can then again release CO_2. Additionally, OFGs integrated in rings or bonded to aromatic rings play an important role in breaking aromatic carbon frameworks. They facilitate the addition of radicals, in particular of OH•, to neighboring carbon atoms. Once the aromaticity of a ring is broken it is easily degraded. This has been observed e.g. for furans, oxepines, quinones, lactones, and pyrones. The perturbation of the aromaticity eases further reactions at the so activated positions which eventually leads to the opening of the carbon rings.

Aldehydes, carboxylic acids, aromatic alcohols, quinones, furans, and dioxines react – in difference to unfunctionalized aromatic compounds like benzene [68] – barrierless with OH• radicals to reactive intermediates with radical sites in aromatic rings. These radical sites can react with molecular oxygen to peroxy radicals which are highly reactive intermediates in combustion that can lead chain branching reactions [69–71]. Through these pathways, oxygen functional groups facilitate the combustion of char by perturbing the aromaticity, activating neighboring carbon atoms, and by opening reaction pathways with low barriers to reactive intermediates and radical chain branching reactions.

Besides the general observations of the atomistic reaction mechanisms of OFGs in char, this work also provides a database of reliable reaction energies and barriers for a wide range of relevant reactions involved in these processes. This dataset can thus serve as a basis for more compact generalized reaction models for char combustion by sensitivity analysis or kinetic Monte Carlo approaches. In addition, combustion rates of (bio)char with different content of specific OFGs can be estimated based on the computed rate parameters. Overall, the results demonstrate that a combined workflow of reactive MD, automated reaction discovery, and refinement by electronic structure methods can provide mechanistic data for combustion modeling beyond mere fitting to often scarce experimental data.

CRediT authorship contribution statement

Özlem Yönder: Writing – original draft, Validation, Investigation, Data curation, Conceptualization. **Gunnar Schmitz:** Writing – review & editing, Methodology. **Rochus Schmid:** Writing – review & editing, Supervision, Project administration, Methodology, Funding acquisition. **Bastian Schnieder:** Writing – review & editing, Data curation. **Christof Hättig:** Writing – review & editing, Supervision, Project administration, Methodology, Funding acquisition, Data curation, Conceptualization.

Declaration of competing interest

The authors declare the following financial interests/personal relationships which may be considered as potential competing interests: Özlem Yönder reports financial support was provided by German Research Foundation. Bastian Schnieder reports financial support was provided by German Research Foundation. Christof Hättig reports a relationship with TURBOMOLE GmbH that includes: equity or stocks. If there are other authors, they declare that they have no known competing financial interests or personal relationships that could have appeared to influence the work reported in this paper.

Data availability

Additional data is available in a Zenodo repository at https://doi.org/10.5281/zenodo.10514181 or on request from the authors.

Acknowledgment

This work has been funded by the Deutsche Forschungsgemeinschaft (DFG, German Research Foundation) – 21503559 – SFB/TRR 129 “Oxyflame”.

Appendix A. Rate constants

Reaction rate constants have been calculated for all reactions with significant barriers using transition state theory as described in detail in Refs. [16,37]. The partition functions have been calculated by a slightly modified quasi-rigid rotor and harmonic oscillator (qRRHO) approximation [37,72] that accounts approximately for hindered internal rotations, with the rotational constants and vibrational frequency from TPSSh-D3/TZVP. The transmission coefficients have been calculated using the high temperature limit of the Eckart tunneling correction [73] with imaginary frequencies from TPSSh-D3/TZVP and electronic activation energies from CCSD(F12*)(T*)/cc-pVDZ-F12. The rate constants were calculated for the temperature range of 300–3000 K and then, for a compact representation of the temperature-dependent results, fitted to the modified Arrhenius expression:

$$k(T) = AT^n \exp(-E/T) \tag{A.1}$$

where T and E are in units of Kelvin. The following tables list the fitted values for $\ln A$, n, and E. The structures for all compounds and transition states and their energies are available in Ref. [74].

A.1. A: Phenanthrene-2-carbaldehyde

See Table A.11.

A.2. B: Phenanthrene-2-carboxylic acid

See Table A.12.

A.3. C: Phenanthrene-2-ol

See Table A.13.

Table A.11
Rate constant parameters for phenanthrene-2-carbaldehyde.

Reaction step	ln A	n	E	Units of $k(T)$
A0 + OH• → A2 + H_2O	Barrierless			
A0 + OH• → A1	11.5	1.908	2752.8	cm^3 mol^{-1} s^{-1}
reverse	29.6	0.1915	10 402.5	1/s
A1 → A2 + H_2O	28.78	0.2197	12 140.2	1/s
reverse	2.97	2.634	17 579.3	cm^3 mol^{-1} s^{-1}
A2 + OH• → A3	Barrierless			
A2 → A4 + CO	Barrierless			
A1 → A4 + formic acid	31.175	−0.00281	5548.07	1/s
reverse	7.278	1.981	2271.61	cm^3 mol^{-1} s^{-1}
A1 → A5	26.31	0.465	8529.4	1/s
reverse	25.2	0.602	8410.5	1/s
A5 → A6 + CHO•	25.7	0.617	20 158.4	1/s
reverse	4.2	2.30	18 540.9	cm^3 mol^{-1} s^{-1}
A5 → A4 + formic acid	32.0	−0.0183	11 349.6	1/s
reverse	9.25	1.85	8192.0	cm^3 mol^{-1} s^{-1}
A1 + OH• → A7 + H_2O	Barrierless			
A7 → A4 + HCO_2•	Barrierless			
A1 → A8	27.04	0.4448	13 506.32	1/s
reverse	27.06	0.3159	13 185.64	1/s
A8 → A6 + CHO•	27.73	0.3418	7208.44	1/s
reverse	5.31	2.27	5945.0	cm^3 mol^{-1} s^{-1}
A6 + CHO• → A9	7.99	1.9348	4507.64	cm^3 mol^{-1} s^{-1}
reverse	28.73	0.2903	9342.89	1/s
A9 + O_2 → A10 + HO_2•	Barrierless			
A10 → A11	27.92	0.3783	13 733.61	1/s
reverse	23.17	0.6626	5978.01	1/s

Table A.12
Rate constant parameters for phenanthrene-2-carboxylic acid.

Reaction step	ln A	n	E	Units of $k(T)$
B0 + OH• → B1 + H_2O	Barrierless			
B1 → B2 + CO_2	30.43	0.1467	2693.96	1/s
reverse	6.01	2.5282	4573.43	cm^3 mol^{-1} s^{-1}
B2 + O_2 → B3	Barrierless			

Table A.13
Rate constant parameters for phenanthrene-2-ol.

Reaction step	ln A	n	E	Units of $k(T)$
C0 + OH• → C1 + H_2O	Barrierless			
C1 + OH• → C2	Barrierless			
C2 + OH• → C3 + H_2O	Barrierless			
C3 → C4	27.83	0.4218	3481.47	1/s
reverse	27.57	0.5386	22 894.05	1/s
C2 → C5	28.08	0.3990	18 327.11	1/s
reverse	21.14	0.8241	11 083.01	1/s
C0 + OH• → C6	Barrierless			
C6 → C7	26.02	0.5200	16 366.18	1/s
reverse	28.82	0.1731	5099.40	1/s
C7 → C8	29.40	0.1293	6178.90	1/s
reverse	24.86	0.6374	7539.18	1/s

A.4. D: Naphtho[1,2-c]furan-1,3-dione

See Table A.14.

A.5. E: Dibenzo[c,e]oxepine-5,7-dione

See Table A.15.

A.6. F: Phenanthrene-9,10-dione

See Table A.16.

A.7. G: Dibenzo[b,d]furan

See Table A.17.

A.8. H: Dibenzo[b,e]dioxine

See Table A.18.

A.9. I: Naptho[2,1-b]furan-2(1H)-one

See Table A.19.

Table A.14
Rate constant parameters for naphtho[1,2-c]furan-1,3-dione.

Reaction step	ln A	n	E	Units of $k(T)$
D0 + H_2O → D2	1.95	2.7728	17 868.70	$cm^3\ mol^{-1}\ s^{-1}$
reverse	23.47	0.9296	18 364.54	1/s
D0 + H → D1	17.72	1.6669	13 599.50	$cm^3\ mol^{-1}\ s^{-1}$
reverse	19.41	1.3420	24 162.69	1/s
D1 + OH• → D2	Barrierless			
D2 + OH• → D3 + H_2O	Barrierless			
D3 + OH• → D4-T + H_2O	Barrierless			
D4-T → D5-T + CO_2	30.45	0.1288	1780.82	1/s
reverse	4.96	2.6426	6416.33	$cm^3\ mol^{-1}\ s^{-1}$
D5-T → D6-T + CO_2	30.95	0.0343	4211.58	1/s
reverse	6.41	2.5363	4285.85	$cm^3\ mol^{-1}\ s^{-1}$
D3 + OH• → D4-S + H_2O	Barrierless			
D4-S → D5-S + CO_2	Not calculated			

Table A.15
Rate constant parameters for dibenzo[c,e]oxepine-5,7-dione.

Reaction step	ln A	n	E	Units of $k(T)$
E0 + H → E1	19.15	1.5680	4083.00	$cm^3\ mol^{-1}\ s^{-1}$
reverse	25.51	0.7882	15 531.02	1/s
E1 → E2	29.89	0.0738	5630.34	1/s
reverse	22.33	0.7899	7666.90	1/s
E2 → E3 + OH•	Barrierless			
E0 → E4 + CO_2	26.51	0.6306	26 606.84	1/s
reverse	0.24	3.0888	34 166.34	$cm^3\ mol^{-1}\ s^{-1}$
E0 + OH• → E5	7.18	2.4013	2804.34	$cm^3\ mol^{-1}\ s^{-1}$
reverse	31.23	0.0477	7399.81	1/s
E5 → E6	28.91	0.3403	5376.95	1/s
reverse	15.93	1.6575	12 673.36	1/s

Table A.16
Rate constant parameters for phenanthrene-9,10-dione.

Reaction step	ln A	n	E	Units of $k(T)$
F0 + H_2O → F2	−1.67	3.2377	17 089.78	$cm^3\ mol^{-1}\ s^{-1}$
reverse	27.87	0.4336	22 307.80	1/s
F0 + H → F1	Barrierless			
F1 + OH• → F2	Barrierless			
F1 + OH• → F3	7.85	2.2131	5878.08	$cm^3\ mol^{-1}\ s^{-1}$
reverse	29.74	0.0931	4402.11	1/s
F0 + OH• → F4	Barrierless			
F4 → F5	27.23	0.4072	13 417.58	1/s
reverse	19.56	1.2351	2115.04	1/s

Table A.17
Rate constant parameters for dibenzo[b,d]furan.

Reaction step	ln A	n	E	Units of $k(T)$
G0 + OH• → G1	12.89	1.8359	1471.47	$cm^3\ mol^{-1}\ s^{-1}$
reverse	32.95	−0.1537	10 645.75	1/s
G1 → G2	29.96	0.0539	9277.35	1/s
reverse	23.78	0.6633	13 337.82	1/s
G0 + OH• → G3	Barrierless			

Table A.18
Rate constant parameters for dibenzo[b,e]dioxine.

Reaction step	ln A	n	E	Units of $k(T)$
H0 + OH• → H1	Barrierless			
H1 → H2	30.00	0.0959	9010.60	1/s
reverse	22.81	0.7387	11 243.21	1/s
H3 → H4	28.58	0.2342	5055.29	1/s
reverse	27.27	0.2893	4053.62	1/s
H4 + OH• → H5	Barrierless			
H5 → H6	27.24	0.3894	6657.13	1/s
reverse	24.57	0.4167	4645.79	1/s
H6 → H7	28.69	0.1090	1183.69	1/s
reverse	28.36	0.3351	64.87	1/s
H7 → H8	30.62	0.1881	18 297.96	1/s
reverse	23.25	0.6756	5650.68	1/s
H8 → H9 + H10	38.69	−0.7178	16 070.73	1/s
reverse	10.84	1.2481	4591.58	$cm^3\ mol^{-1}\ s^{-1}$

Table A.19
Rate constant parameters for naptho[2,1-b]furan-2(1H)-one.

Reaction step	ln A	n	E	Units of $k(T)$
I0 → I1 + CO_2	34.26	−0.0069	51 553.08	1/s
reverse	3.56	2.8214	12 208.54	$cm^3\ mol^{-1}\ s^{-1}$
I1 → I2	28.07	0.1948	677.50	1/s
reverse	28.18	0.3203	13 785.89	1/s
I0 + OH• → I4	10.00	2.1191	7163.25	$cm^3\ mol^{-1}\ s^{-1}$
reverse	20.79	1.2329	27 153.63	1/s

Table A.20
Rate constant parameters for 6H-benzo[c]chromen-6-one.

Reaction step	ln A	n	E	Units of $k(T)$
J0 + OH• → J6	8.62	2.1578	4994.20	$cm^3\ mol^{-1}\ s^{-1}$
reverse	23.66	0.7195	19 616.61	1/s
J0 + O → J7	16.76	1.4613	7791.20	$cm^3\ mol^{-1}\ s^{-1}$
reverse	23.04	0.7217	18 169.15	1/s
J0 + OH• → J1	Barrierless			
J1 + O_2 → J2 + HO_2•	9.00	1.8878	4565.87	$cm^3\ mol^{-1}\ s^{-1}$
reverse	5.87	2.2228	16 814.43	$cm^3\ mol^{-1}\ s^{-1}$
J2 + OH• → J3	Barrierless			
J2 + OH• → J8 + H_2O	6.17	2.7558	2863.64	$cm^3\ mol^{-1}\ s^{-1}$
reverse	0.62	3.1344	5637.19	$cm^3\ mol^{-1}\ s^{-1}$
J4 + OH• → J5	9.09	2.1182	4622.19	$cm^3\ mol^{-1}\ s^{-1}$
reverse	25.79	0.5054	21 429.72	1/s

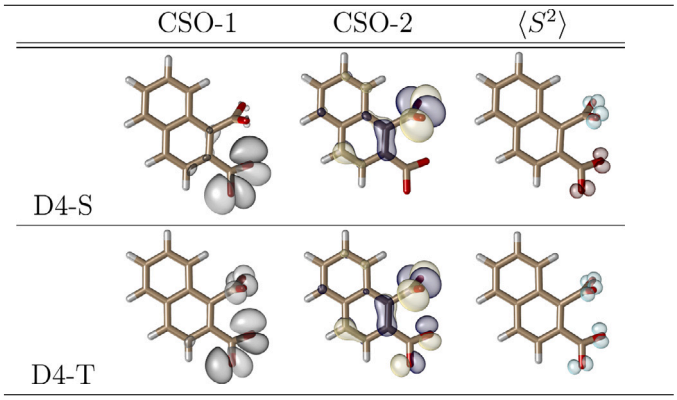
A.10. J: 6H-benzo[c]chromen-6-one

See Table A.20.

Appendix B. The electronic structure of D4-S and D4-T

The Table B.21 shows the singly occupied molecular orbitals (CSO) of open-shell singlet (D4-S) and triplet species (D4-T) as well as the total spin density of the individual molecules.

Table B.21
Spin densities and spin densities of species D4-S and D4-T calculated at level of theory DFT/TPSSh-D3/TZVP.



References

[1] Locaspi A, Debiagi P, Pelucchi M, Hasse C, Faravelli T. A predictive physico-chemical model of biochar oxidation. Energy Fuels 2021;35(18):14894–912. http://dx.doi.org/10.1021/acs.energyfuels.1c01559.

[2] Jenkins RW, Moore CM, Semelsberger TA, Chuck CJ, Gordon JC, Sutton AD. The effect of functional groups in bio-derived fuel candidates. ChemSusChem 2016;9(9):922–31. http://dx.doi.org/10.1002/cssc.201600159.

[3] Sankar M, Nowicka E, Carter E, Murphy DM, Knight DW, Bethell D, Hutchings GJ. The benzaldehyde oxidation paradox explained by the interception of peroxy radical by benzyl alcohol. Nature Commun 2014;5(1):3332. http://dx.doi.org/10.1038/ncomms4332.

[4] Nowakowska M, Herbinet O, Dufour A, Glaude PA. Kinetic study of the pyrolysis and oxidation of guaiacol. J Phys Chem A 2018;122(39):7894–909. http://dx.doi.org/10.1021/acs.jpca.8b06301.

[5] Brennan JK, Bandosz TJ, Thomson KT, Gubbins KE. Water in porous carbons. Colloids Surf A 2001;187–188:539–68. http://dx.doi.org/10.1016/S0927-7757(01)00644-6.

[6] Keiluweit M, Nico PS, Johnson MG, Kleber M. Dynamic molecular structure of plant biomass-derived black carbon (Biochar). Environ Sci Technol 2010;44(4):1247–53. http://dx.doi.org/10.1021/es9031419.

[7] Turner J, Thomas K, Russell A. The identification of oxygen functional groups in carbonaceous materials by oxygen K-edge XANES. Carbon 1997;35(7):983–92. http://dx.doi.org/10.1016/S0008-6223(97)00054-7.

[8] Simm GN, Reiher M. Context-driven exploration of complex chemical reaction networks. J Chem Theory Comput 2017;13(12):6108–19. http://dx.doi.org/10.1021/acs.jctc.7b00945.

[9] Unsleber JP, Grimmel SA, Reiher M. Chemoton 2.0: Autonomous exploration of chemical reaction networks. J Chem Theory Comput 2022;18(9):5393–409. http://dx.doi.org/10.1021/acs.jctc.2c00193.

[10] Grimme S. Exploration of chemical compound, conformer, and reaction space with meta-dynamics simulations based on tight-binding quantum chemical calculations. J Chem Theory Comput 2019;15(5):2847–62. http://dx.doi.org/10.1021/acs.jctc.9b00143.

[11] Castro-Marcano F, Kamat AM, Russo MF, van Duin AC, Mathews JP. Combustion of an Illinois No. 6 coal char simulated using an atomistic char representation and the ReaxFF reactive force field. Combust Flame 2012;159(3):1272–85. http://dx.doi.org/10.1016/j.combustflame.2011.10.022.

[12] van Duin ACT, Dasgupta S, Lorant F, Goddard WA. ReaxFF: A reactive force field for hydrocarbons. J Phys Chem A 2001;105(41):9396–409. http://dx.doi.org/10.1021/jp004368u.

[13] Chenoweth K, van Duin ACT, Goddard WA. ReaxFF reactive force field for molecular dynamics simulations of hydrocarbon oxidation. J Phys Chem A 2008;112(5):1040–53. http://dx.doi.org/10.1021/jp709896w.

[14] Döntgen M, Przybylski-Freund M-D, Kröger LC, Kopp WA, Ismail AE, Leonhard K. Automated discovery of reaction pathways, rate constants, and transition states using reactive molecular dynamics simulations. J Chem Theory Comput 2015;11(6):2517–24. http://dx.doi.org/10.1021/acs.jctc.5b00201.

[15] Döntgen M, Schmalz F, Kopp WA, Kröger LC, Leonhard K. Automated chemical kinetic modeling via hybrid reactive molecular dynamics and quantum chemistry simulations. J Chem Inf Model 2018;58(7):1343–55. http://dx.doi.org/10.1021/acs.jcim.8b00078.

[16] Schmitz G, Yönder Ö, Schnieder B, Schmid R, Hättig C. An automatized workflow from molecular dynamic simulation to quantum chemical methods to identify elementary reactions and compute reaction constants. J Comput Chem 2021;42(32):2264–82. http://dx.doi.org/10.1002/jcc.26757.

[17] Plimpton S. Fast parallel algorithms for short-range molecular dynamics. J Comput Phys 1995;117(1):1–19. http://dx.doi.org/10.1006/jcph.1995.1039.

[18] Aktulga HM, Fogarty JC, Pandit SA, Grama AY. Parallel reactive molecular dynamics: Numerical methods and algorithmic techniques. Parallel Comput 2012;38(4–5):245–59. http://dx.doi.org/10.1016/j.parco.2011.08.005.

[19] Balasubramani SG, Chen GP, Coriani S, Diedenhofen M, Frank MS, Franzke YJ, Furche F, Grotjahn R, Harding ME, Hättig C, Hellweg A, Helmich-Paris B, Holzer C, Huniar U, Kaupp M, Khah AM, Khani SK, Mueller T, Mack F, Nguyen BD, Parker SM, Perlt E, Rappoport D, Reiter K, Roy S, Rückert M, Schmitz G, Sierka M, Tapavicza E, Tew DP, van Wuellen C, Voora VK, Weigend F, Wodynski A, Yu JM. TURBOMOLE: Modular program suite for ab initio quantum-chemical and condensed-matter simulations. J Chem Phys 2020;152(18). http://dx.doi.org/10.1063/5.0004635.

[20] TURBOMOLE V7.6 2021, a development of University of Karlsruhe and Forschungszentrum Karlsruhe GmbH, 1989–2007. TURBOMOLE GmbH; 2021, since 2007; available from https://www.turbomole.org.

[21] TURBOMOLE V7.7 2022, a development of University of Karlsruhe and Forschungszentrum Karlsruhe GmbH, 1989–2007. TURBOMOLE GmbH; 2022, since 2007; available from https://www.turbomole.org.

[22] Grimme S, Antony J, Ehrlich S, Krieg H. A consistent and accurate ab-initio parametrization of density functional dispersion correction (DFT-D) for the 94 elements H-Pu. J Chem Phys 2010;132(15):154104. http://dx.doi.org/10.1063/1.3382344.

[23] Tao J, Perdew JP, Staroverov VN, Scuseria GE. Climbing the density functional ladder: Nonempirical meta generalized gradient approximation designed for molecules and solids. Phys Rev Lett 2003;91:146401. http://dx.doi.org/10.1103/PhysRevLett.91.146401.

[24] Schäfer A, Horn H, Ahlrichs R. Fully optimized contracted Gaussian basis sets for atoms Li to Kr. J Chem Phys 1992;97(4):2571–7.

[25] Eichkorn K, Treutler O, Öhm H, Häser M, Ahlrichs R. Auxiliary basis sets to approximate Coulomb potentials. Chem Phys Lett 1995;240(4):283–90. http://dx.doi.org/10.1016/0009-2614(95)00621-A.

[26] Staroverov VN, Scuseria GE, Tao J, Perdew JP. Comparative assessment of a new nonempirical density functional: Molecules and hydrogen-bonded complexes. J Chem Phys 2003;119(23):12129–37. http://dx.doi.org/10.1063/1.1626543.

[27] Schäfer A, Huber C, Ahlrichs R. Fully optimized contracted Gaussian basis sets of triple zeta valence quality for atoms Li to Kr. J Chem Phys 1994;100(8):5829–35. http://dx.doi.org/10.1063/1.467146.

[28] Eichkorn K, Weigend F, Treutler O, Ahlrichs R. Auxiliary basis sets for main row atoms and transition metals and their use to approximate Coulomb potentials. Theor Chem Account 1997;97(1):119–24. http://dx.doi.org/10.1007/s002140050244.

[29] Csonka GI, Ruzsinszky A, Perdew JP. Estimation, computation, and experimental correction of molecular zero-point vibrational energies. J Phys Chem A 2005;109(30):6779–89. http://dx.doi.org/10.1021/jp0519464.

[30] Hättig C, Tew DP, Köhn A. Communications: Accurate and efficient approximations to explicitly correlated coupled-cluster singles and doubles, CCSD-F12. J Chem Phys 2010;132(23):231102. http://dx.doi.org/10.1063/1.3442368.

[31] Marchetti O, Werner H-J. Accurate calculations of intermolecular interaction energies using explicitly correlated wave functions. Phys Chem Chem Phys 2008;10:3400–9. http://dx.doi.org/10.1039/B804334E.

[32] Häser M, Ahlrichs R. Improvements on the direct SCF method. J Comput Chem 1989;10(1):104–11. http://dx.doi.org/10.1002/jcc.540100111.

[33] Peterson KA, Adler TB, Werner H-J. Systematically convergent basis sets for explicitly correlated wavefunctions: The atoms H, He, B–Ne, and Al–Ar. J Chem Phys 2008;128(8):084102. http://dx.doi.org/10.1063/1.2831537.

[34] Hättig C. Optimization of auxiliary basis sets for RI-MP2 and RI-CC2 calculations: Core–valence and quintuple-ζ basis sets for H to Ar and QZVPP basis sets for Li to Kr. Phys Chem Chem Phys 2005;7:59–66. http://dx.doi.org/10.1039/B415208E.

[35] Weigend F, Köhn A, Hättig C. Efficient use of the correlation consistent basis sets in resolution of the identity MP2 calculations. J Chem Phys 2002;116(8):3175–83. http://dx.doi.org/10.1063/1.1445115.

[36] Yousaf KE, Peterson KA. Optimized auxiliary basis sets for explicitly correlated methods. J Chem Phys 2008;129(18):184108. http://dx.doi.org/10.1063/1.3009271.

[37] Yönder Ö, Hättig C. Density functional theory study of CO formation through reactions of polycyclic aromatic hydrocarbons with atomic oxygen ($O(^3P)$). Fuel 2019;241:851–60. http://dx.doi.org/10.1016/j.fuel.2018.12.047.

[38] Westbrook CK. Chemical kinetics of hydrocarbon ignition in practical combustion systems. Proc Combust Inst 2000;28(2):1563–77. http://dx.doi.org/10.1016/S0082-0784(00)80554-8.

[39] Marinov NM. A detailed chemical kinetic model for high temperature ethanol oxidation. Int J Chem Kinet 1999;31(3):183–220. http://dx.doi.org/10.1002/(SICI)1097-4601(1999)31:3<183::AID-KIN3>3.0.CO;2-X.

[40] Otake Y, Jenkins RG. Characterization of oxygen-containing surface complexes created on a microporous carbon by air and nitric acid treatment. Carbon 1993;31(1):109–21. http://dx.doi.org/10.1016/0008-6223(93)90163-5.

[41] Salooja K. The role of aldehydes in combustion: Studies of the combustion characteristics of aldehydes and of their influence on hydrocarbon combustion processes. Combust Flame 1965;9(4):373–82. http://dx.doi.org/10.1016/0010-2180(65)90026-X.

[42] Namysl S, Pelucchi M, Pratali Maffei L, Herbinet O, Stagni A, Faravelli T, Battin-Leclerc F. Experimental and modeling study of benzaldehyde oxidation. Combust Flame 2020;211:124–32. http://dx.doi.org/10.1016/j.combustflame.2019.09.024.

[43] Qi X, Li Y, Chen L, Tang J, Xin H, Liang Z. Reaction mechanism of aldehyde groups during coal self-heating. ACS Omega 2020;5(36):23184–92.

[44] Eskay TP, Britt PF, Buchanan AC. Pyrolysis of aromatic carboxylic acids: Potential involvement of anhydrides in retrograde reactions in low-rank coal. Energy Fuels 1997;11(6):1278–87. http://dx.doi.org/10.1021/ef9700745.

[45] Cartlidge J, Tipper CFH, Bawn CEH. The peroxides formed during hydrocarbon slow combustion and their role in the mechanism. Proc R Soc Lond Ser A 1961;261(1306):388–401. http://dx.doi.org/10.1098/rspa.1961.0085.

[46] Walling C, Savas ES. The reaction of phenyl radicals with carbon monoxide; some observations on the induced decomposition of Benzoyl Peroxide1. J Am Chem Soc 1960;82(7):1738–44. http://dx.doi.org/10.1021/ja01492a050.

[47] Frassoldati A, Cuoci A, Faravelli T, Niemann U, Ranzi E, Seiser R, Seshadri K. An experimental and kinetic modeling study of n-propanol and iso-propanol combustion. Combust Flame 2010;157(1):2–16. http://dx.doi.org/10.1016/j.combustflame.2009.09.002.

[48] Du X, Fan H, Liu S, Zhang ZC. Selective nucleophilic α-C alkylation of phenols with alcohols via Ti=cα intermediate on anatase TiO2 surface. Nature Commun 2023;14(1):4479. http://dx.doi.org/10.1038/s41467-023-40101-7.

[49] Nguyen TL, Peeters J, Vereecken L. Theoretical reinvestigation of the $O(^3P)$ + C_6H_6 reaction: Quantum chemical and statistical rate calculations. J Phys Chem A 2007;111(19):3836–49. http://dx.doi.org/10.1021/jp0660886.

[50] Taatjes CA, Osborn DL, Selby TM, Meloni G, Trevitt AJ, Epifanovsky E, Krylov AI, Sirjean B, Dames E, Wang H. Products of the benzene + $O(^3P)$ reaction. J Phys Chem A 2010;114(9):3355–70. http://dx.doi.org/10.1021/jp9114145.

[51] Bond GC. Mechanism of the oxidation of o-xylene to phthalic anhydride. J Catal 1989;116(2):531–9. http://dx.doi.org/10.1016/0021-9517(89)90119-X.

[52] de Munck NA, Richter O, Eberle H-J, Mestl G. Oxidation of o -xylene and naphthalene to phthalic anhydride. In: Industrial arene chemistry. John Wiley & Sons, Ltd; 2023, p. 1153–202. http://dx.doi.org/10.1002/9783527827992.ch39, (Chapter 39).

[53] da Silva G, Chen C-C, Bozzelli JW. Toluene combustion: Reaction paths, thermochemical properties, and kinetic analysis for the methylphenyl radical + O_2 reaction. J Phys Chem A 2007;111(35):8663–76. http://dx.doi.org/10.1021/jp068640x.

[54] Rezgui Y, Guemini M. Benzene combustion: A detailed chemical kinetic modeling in laminar flames conditions. Kinet Catal 2014;55(3):278–86. http://dx.doi.org/10.1134/S0023158414030124.

[55] Dagaut P. Kinetics of oxygen-containing organic compounds with hydroxyl radicals in the gas phase : a review for modeling combustion and atmospheric chemistry. J Chim Phys 1989;86:595–623. http://dx.doi.org/10.1051/jcp/1989860595.

[56] Wu S, Tay KL, Li J, Yang W, Yang S. Development of a compact and robust kinetic mechanism for furan group biofuels combustion in internal combustion engines. Fuel 2021;298:120824. http://dx.doi.org/10.1016/j.fuel.2021.120824.

[57] Hu B, Warczinski L, Li X, Lu M, Bitzer J, Heidelmann M, Eckhard T, Fu Q, Schulwitz J, Merko M, Li M, Kleist W, Hättig C, Muhler M, Peng B. Formic acid-assisted selective hydrogenolysis of 5-hydroxymethylfurfural to 2,5-dimethylfuran over bifunctional Pd nanoparticles supported on N-doped mesoporous carbon. Angew Chem Int Ed 2021;60(12):6807–15. http://dx.doi.org/10.1002/anie.202012816.

[58] Xu N, Gong J, Huang Z. Review on the production methods and fundamental combustion characteristics of furan derivatives. Renew Sustain Energy Rev 2016;54:1189–211. http://dx.doi.org/10.1016/j.rser.2015.10.118.

[59] Tay KL, Yang W, Zhao F, Lin Q, Wu S. Development of a highly compact and robust chemical reaction mechanism for unsaturated furan oxidation in internal combustion engines via a multiobjective genetic algorithm and generalized polynomial chaos. Energy Fuels 2020;34(1):936–48. http://dx.doi.org/10.1021/acs.energyfuels.9b03272.

[60] Jouzdani S, Eldeeb MA, Zhang L, Akih-Kumgeh B. High-temperature study of 2-methyl furan and 2-methyl tetrahydrofuran combustion. Int J Chem Kinet 2016;48(9):491–503. http://dx.doi.org/10.1002/kin.21008.

[61] Vogg H, Metzger M, Stieglitz L. Recent findings on the formation and decomposition of pcdd/pcdf in municipal solid waste incineration**presented at the ISWA–WHO–DAKOFA specialized seminar, emission of trace organics from municipal solid waste incinerators, copenhagen, 20–22 january 1987. In: Dean RB, editor. Incineration of municipal waste. Academic Press; 1988, p. 207–16. http://dx.doi.org/10.1016/B978-0-12-207690-9.50022-2.

[62] Marquaire P-M, Bounaceur R, Baronnet F. Detailed mechanism of dibenzofuran oxidation. Organohalogen Compds 2003;63:377–80.

[63] Ziegler-Devin I, Bounaceur R, Perrin C, Wörner R, Patisson F, Marquaire P. Kinetic study of abatement of low concentration of dibenzofuran by oxidation – Effects of co-reactants. Chem Eng J 2013;218:154–63. http://dx.doi.org/10.1016/j.cej.2012.12.023.

[64] Tritz A, Ziegler-Devin I, Perrin C, Marquaire P-M. Experimental study of the oxidation and pyrolysis of dibenzofuran at very low concentration. J Environ Chem Eng 2014;2(1):143–53. http://dx.doi.org/10.1016/j.jece.2013.11.030.

[65] Zeng X, Zhang X, Wang Z. Theoretical study on the OH-initiated oxidation mechanism of polyfluorinated dibenzo-p-dioxins under the atmospheric conditions. Chemosphere 2016;144:2036–43. http://dx.doi.org/10.1016/j.chemosphere.2015.10.106.

[66] Bloss C, Wagner V, Jenkin ME, Volkamer R, Bloss WJ, Lee JD, Heard DE, Wirtz K, Martin-Reviejo M, Rea G, Wenger JC, Pilling MJ. Development of a detailed chemical mechanism (MCMv3.1) for the atmospheric oxidation of aromatic hydrocarbons. Atmos Chem Phys 2005;5(3):641–64. http://dx.doi.org/10.5194/acp-5-641-2005.

[67] Jin Z-H, Yu D, Liu Y-X, Tian Z-Y, Richter S, Braun-Unkhoff M, Naumann C, Yang J-Z. An experimental investigation of furfural oxidation and the development of a comprehensive combustion model. Combust Flame 2021;226:200–10. http://dx.doi.org/10.1016/j.combustflame.2020.12.015.

[68] Vourliotakis G, Skevis G, Founti MA. A detailed kinetic modeling study of benzene oxidation and combustion in premixed flames and ideal reactors. Energy Fuels 2011;25(5):1950–63. http://dx.doi.org/10.1021/ef101712p.

[69] Wang Z, Ehn M, Rissanen MP, Garmash O, Quéléver L, Xing L, Monge-Palacios M, Rantala P, Donahue NM, Berndt T, Sarathy SM. Efficient alkane oxidation under combustion engine and atmospheric conditions. Commun Chem 2021;4(1):18. http://dx.doi.org/10.1038/s42004-020-00445-3.

[70] Goldman MJ, Green WH, Kroll JH. Chemistry of simple organic peroxy radicals under atmospheric through combustion conditions: Role of temperature, pressure, and NOx level. J Phys Chem A 2021;125(48):10303–14. http://dx.doi.org/10.1021/acs.jpca.1c07203.

[71] Suh I, Zhang R, Molina LT, Molina MJ. Oxidation mechanism of aromatic peroxy and bicyclic radicals from OH-toluene reactions. J Am Chem Soc 2003;125(41):12655–65. http://dx.doi.org/10.1021/ja0350280.

[72] Grimme S. Supramolecular binding thermodynamics by dispersion-corrected density functional theory. Chem – Eur J 2012;18(32):9955–64. http://dx.doi.org/10.1002/chem.201200497.

[73] Shavitt I. A calculation of the rates of the Ortho-Para conversions and isotope exchanges in Hydrogen. J Chem Phys 1959;31(5):1359–67. http://dx.doi.org/10.1063/1.1730599.

[74] Yönder Ö, Schmitz G, Schmid R, Schnieder B, Hättig C. Raw data to “A computational chemistry study on the evolution of oxygen functional groups during char burnout”. 2024, http://dx.doi.org/10.5281/zenodo.10514181.